Supplementary Information (SI) for Nanoscale.

# Supporting Information

## Optical anisotropy of $Bi_2SeO_5$ and near-field characterization of the waveguide modes

Jinglin Tang, Yaolong Li*, Jingyue Wang*, Yongchao Zhu, Xiaofang Li, Pengzuo Jiang, Jingying Xiao, Yuxin Zhang, Qinyun Liu, Minghao Deng, Guanyu Zhang, Zini Cao, Shufeng Wang, Hong Yang, Xiaoyong Hu*, Han Gao*, Hailin Peng*, Guowei Lyu*, & Qihuang Gong

*Corresponding author. Email: yaolong@pku.edu.cn (Y.L.), 20240072@upc.edu.cn (J.W.), gaohan22@sdjzu.edu.cn (H.G.), xiaoyonghu@pku.edu.cn (X.H.), hlpeng@pku.edu.cn (H.P.), guowei.lu@pku.edu.cn (G.L.).

**Table of Contents**

## 1. Details of the single crystal synthesis of $Bi_2SeO_5$

The prereacted $Bi_2SeO_5$ powder was synthesized from $Bi_2O_3$ powder (Alfa Aesar, 99.999%) and $SeO_2$ powder (Alfa Aesar, 99.999%) with the molar ratio of 1:1. They were sealed in an evacuated quartz tube under vacuum and fed into a furnace (850 °C) for 12 h. For the growth of $Bi_2SeO_5$ single crystals, as-synthesized $Bi_2SeO_5$ powder was mixed with 1.5 mg cm$^{-3}$ $I_2$ crystals (Energy Chemical, sublimated at 120 °C) and resealed in another evacuated quartz tube. The mixed powder was placed in the hot centre of the furnace at 860 °C for 40 d and the $Bi_2SeO_5$ single crystals were recrystallized at the low-temperature zone by $I_2$ transport.

## 2. Polarization-dependent Raman spectra

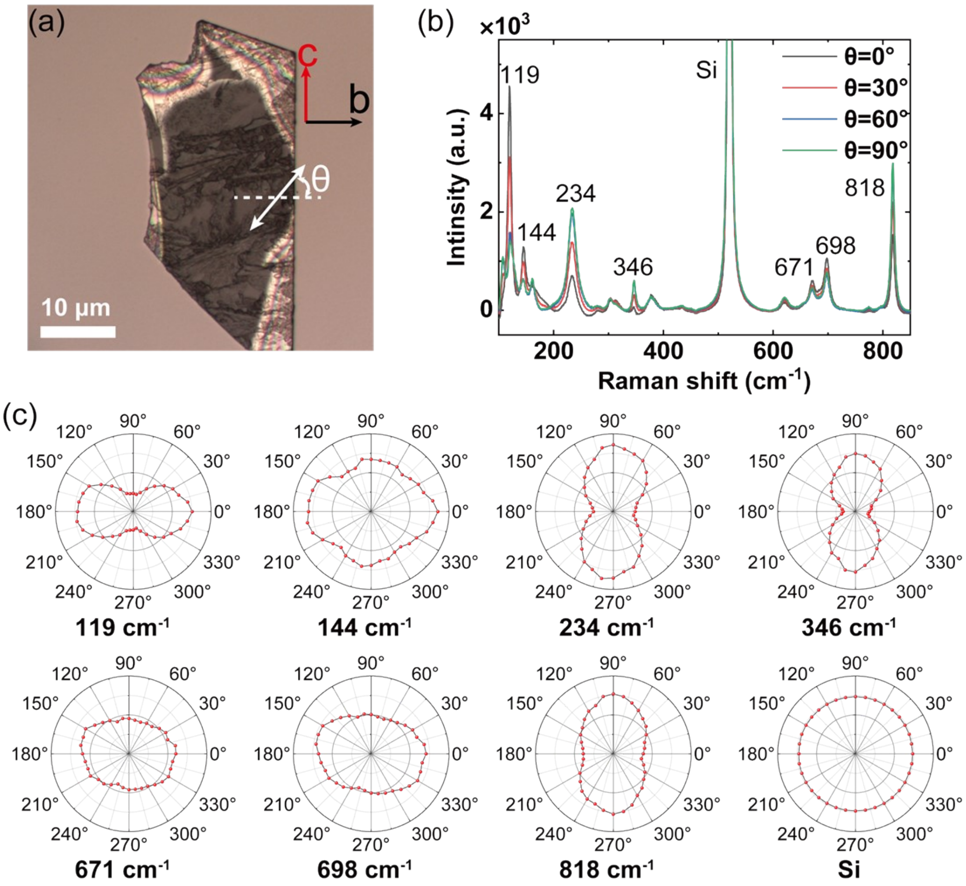

**Figure S1 Polarization-dependent Raman spectra.** (a) optical image of a representative sample. The 2 $\mu$m-thick $Bi_2SeO_5$ sample is transferred on Si substrate, and the crystal axes are marked in the inset. (b) Raman spectra at several different polarizations. (c) Polar plot of representative Raman peaks as a function of polarization angles. The signal of Si is shown for comparison.

We have measured Raman spectra of $Bi_2SeO_5$, as shown in Figure S1. The sample was newly prepared because the signal is too weak to be measured for 100 nm thin film. The

$Bi_2SeO_5$ flake was transferred onto a Si substrate, and the thickness is ~2 $\mu$m measured by AFM. Sharp boundary can be observed, which corresponds to the crystallographic axis. For Raman measurement, we changed the polarization of incident laser (532 nm,12 mW), and the measurements were performed by rotating the incident polarization (controlled by a λ/2 plate) while collecting all scattered polarizations. Each spectrum was recorded with 120 s integration time and averaged over 2 acquisitions. We measured the Raman spectra at different polarization angles (Figure S1b), where the peak positions are 119, 144, 234, 346, 671, 698, 818 $cm^{-1}$, and their signal intensities vary with polarization, as shown in Figure S1c. The signal of Si is shown for comparison, which is near unchanged with polarization angle, demonstrating that the variation of the Raman signal intensity stems from the anisotropy of the material itself. The Raman intensity of these peaks exhibits a distinct two-lobed polarization dependence, demonstrating anisotropic polarizability of the corresponding vibrational modes. Moreover, the orientation of the major and minor axes of the two-lobed profiles suggests that the principal crystallographic axes are aligned with the horizontal and vertical directions of the laboratory frame, consistent with the discussions above.

## 3. DFT calculations of $Bi_2SeO_5$

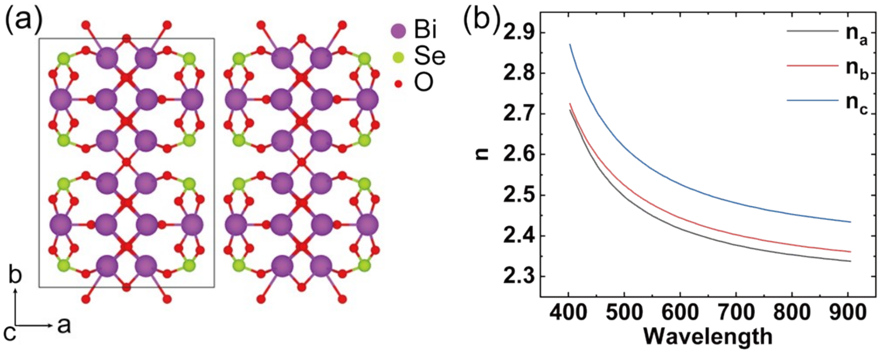

**Figure S2 DFT calculations of $Bi_2SeO_5$.** (a) Theoritical crystal of $Bi_2SeO_5$. Crystal axes are marked in the inset, where c axis is perpendicular to the plane. (b) Calculated refractive index of $Bi_2SeO_5$ ranging from 400 nm to 900 nm.

We have performed DFT calcularions using the PBE functional to calculate the refractive index of $Bi_2SeO_5$. For semiconductors and insulators, the PBE functional could provide a good qualitative description of the electronic structure, but underestimates the overall band gap and consequently overestimates the refractive index. The GW + BSE methods based on many-body perturbation theory could give more accurate values, but require significantly higher computational cost.

## 4. Analytical method of three-layer planar waveguide

Figure S3a shows the structure of a three-planar waveguide. The thickness of $Bi_2SeO_5$ is $h$, which is anisotropic. In our experiment, the thickness of ITO is very thin (~13 nm). Assuming that ITO can be ignored, this structure can be reduced to a three-layer waveguide, and the electric field distribution and dispersion can be resolved using Maxwell's equations and boundary conditions.

In order to distinguish the direction of propagation from the direction of the principal axis of the material, we define the x-, y- and z- axis as the optical principal axes of $Bi_2SeO_5$, and the X-, Y- and Z- axes as the axes of the field components, where X-axis is along the direction of the waveguide propagation, the Y-axis is the in-plane axis perpendicular to the X-axis, and the Z-axis is out-of-plane.The electric field can be written as $E(X, Y, Z) = E(Z)exp[-i(\omega t - \beta X)]$, where $\omega$ and $\beta$ denote angular frequency and propagation constant. Using Maxwell's equations, the electromagnetic fields of TE mode satisfy the relations below:

$$i\beta E_Y =- i\omega\mu_0 H_Z$$

$$\frac{\partial}{\partial Z}E_Y =- i\omega\mu_0 H_X$$

$$\frac{\partial}{\partial Z}H_X - i\beta H_Z -= i\omega\varepsilon_Y E_Y$$

And the electric fields of TE modes in three regions can be written as

$$E_1 = A_1 exp\left(\kappa_1 Z\right), Z < 0$$

$$E_2 = A_2 cos\left(k_{TE}Z - \varphi\right), 0 < Z < h$$

$$E_3 = A_3 exp\left(-\kappa_2 Z\right), Z > h$$

Where $A_1$, $A_2$ and $A_3$ are electric field amplitudes in each region, and $\varphi$ is the phase shift. $\kappa_1 = \sqrt{\beta^2 - k_0^2\varepsilon_1\mu_1}$, $\kappa_2 = \sqrt{\beta^2 - k_0^2\varepsilon_2\mu_2}$, $k_{TE} = \sqrt{k_0^2\varepsilon_Y - \beta^2}$, where $k_0 = \omega/c$. Using boundary condition at $Z = 0$ and $Z = h$, the dispersion relation of TE modes can be obtained as follow

$$k_{TE}h = arctan\left(k_1/k_{TE}\right) + arctan\left(k_2/k_{TE}\right) + m\pi$$

Similarly, the dispersion relation of TM modes can be obtained as follow

$$k_{TM}h = arctan\left(k_1\varepsilon_Z/\varepsilon_1 k_{TM}\right) + arctan\left(k_2\varepsilon_Z/\varepsilon_2 k_{TM}\right) + m\pi$$

Where $k_{TE} = \sqrt{k_0^2\varepsilon_Z - \beta^2\varepsilon_Z/\varepsilon_X}$. According to the functions above, the TE mode is mainly influenced by $\varepsilon_Y$, while the TM mode is both influenced by $\varepsilon_X$ and $\varepsilon_Z$. The calculated results are shown in Figure S3b and S3c, which are consistent with the experimental results in general.

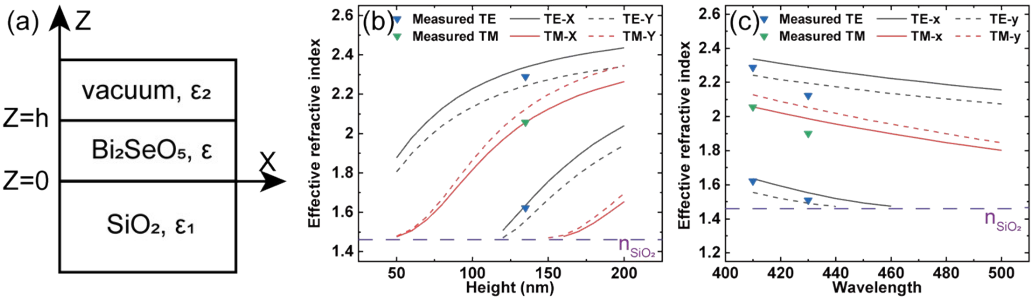

**Figure S3 Analytical method of three-layer planar waveguide.** (a) Schematic of the three-layer planar waveguide. (b) $n_{\text{eff}}$ changing with thickness at 410 nm. (c) $n_{\text{eff}}$ changing with wavelength of incident light at $h$=135 nm. The TE and TM modes are propagating along different principal axes, which are marked as TE-x, TM-x, TE-y and TM-y, respectively. The purple dotted lines correspond to the refractive index of the glass substrate.

## 5. AFM measurement of $Bi_2SeO_5$

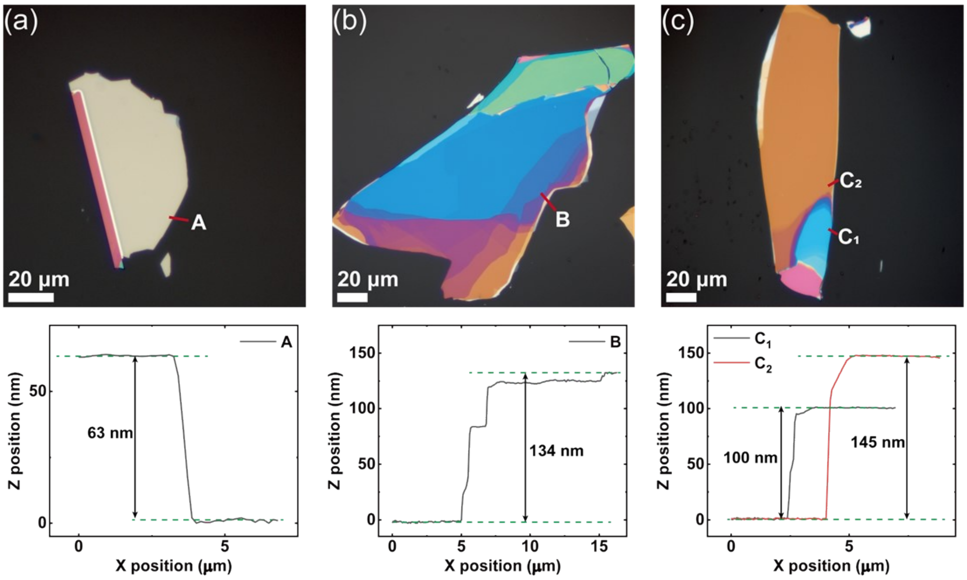

**Figure S4 AFM measurement of $Bi_2SeO_5$ samples.** (a-c) Optical images of samples and corresponding AFM measurements.

## 6. Influence of rotation angle between propagation direction and the principal axis

$Bi_2SeO_5$ is an anisotropic material, and its relative dielectric tensor can be written as

$$\|\varepsilon\| = \begin{bmatrix} \varepsilon_x & 0 & 0 \\ 0 & \varepsilon_y & 0 \\ 0 & 0 & \varepsilon_z \end{bmatrix}$$

Where $\varepsilon_x$, $\varepsilon_y$ and $\varepsilon_z$ are the relative dielectric constants along three principal axes. As noted above, to establish a clear coordinate system, we define the direction of three principal axes

$(x,y,z)$ and direction of waveguide propagation $(X, Y, Z)$. Then, $\theta$ is defined as the rotate angle between the x- and X-axes, and the relative dielectric tensor in X-Y-Z axes becomes

$$\|\varepsilon'\| = \begin{bmatrix} \varepsilon_{xx} & \varepsilon_{xy} & 0 \\ \varepsilon_{yx} & \varepsilon_{yy} & 0 \\ 0 & 0 & \varepsilon_{zz} \end{bmatrix}$$

Where

$$\varepsilon_{xx} = \varepsilon_x \cos^2\theta + \varepsilon_y \sin^2\theta$$

$$\varepsilon_{xy} = \varepsilon_{yx} = (\varepsilon_x - \varepsilon_y)\sin\theta\cos\theta$$

$$\varepsilon_{yy} = \varepsilon_x \sin^2\theta + \varepsilon_y \cos^2\theta$$

$$\varepsilon_{zz} = \varepsilon_z$$

The refractive index measured by spectroscopic ellipsometer is shown in Figure 1. As the principal axes are consistent with the edge of the sample, and the x-axis is confirmed by comparing the color, $\theta$ is estimated to be 25°. FDTD simulations of $n_{\mathrm{eff}}$ changing with thickness at $\theta = 25°$ is shown in Figure S5b, which fit well with the measured results.

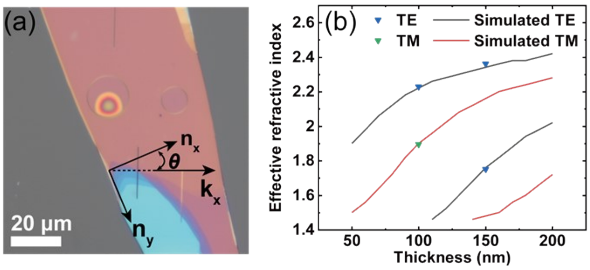

**Figure S5 Influence of rotation angle ($\theta$).** (a) Optical image of the selcted sample, and the axes are marked in the figure. (b) $n_{\mathrm{eff}}$ changing with thickness at $\theta = 25°$ simulated by FDTD.

## 7. PEEM images for line slit excited by laser at different wavelengths

Figure S6a and S6b show the slit excited at 410 nm and 430 nm respectively, and the selected sample is the 134 nm thick sample. The PE intensity signals along the propagation directions are shown in Figure S6c, data of 410 nm are shifted for better comparison. The signal of 430 nm is weaker, and the loss is higher than that of 410 nm, showing that waveguide mode can be excited more easily at shorter wavelength. The $n_{\mathrm{eff}}$ of 430 nm also fits well with simulated results in Figure 2c.

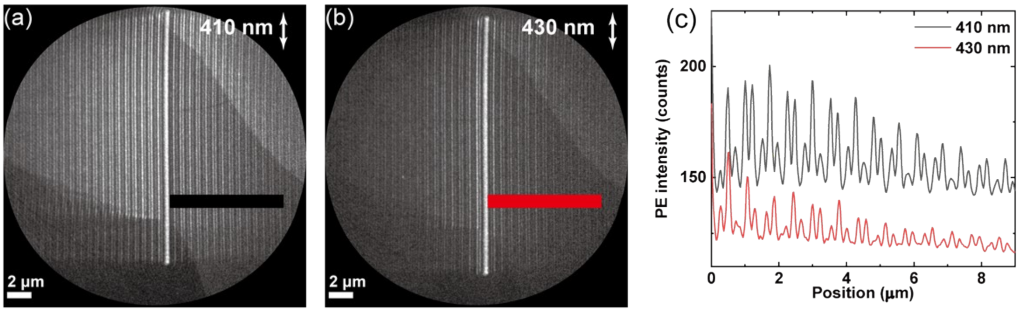

**Figure S6 PEEM images for line slit excited by laser at different wavelengths**. (a, b) PEEM images of the slit excited at (a) 410 nm and (b) 430 nm. The polarization is along the slit. (c) The PE intensity distribution corresponds to the corresponding line in (a, b). The average range in the vertical direction is 2.5 μm (not drawn to scale in the image), and the data of 410 nm are shifted for better comparison.

## 8. Fast Fourier transform results of PEEM images of ring slit

Figure S7 shows the FFT results of $Bi_2SeO_5$ with ring slits. The PEEM images of different polarizations are shown in Figure S7a and S7e. When the laser irradiates onto the sample, the waveguide modes are selectively excited from the ring slit and interfere in the centre, and the responding FFT results are shown in Figure S7b and S7f. Two ellipses can be observed in the FFT results, and the main axes of the ellipses are marked in the figure, corresponding to the principal axes of the refractive index. This result is not obvious, but still different from that of the isotropic material. To show the difference, we present the FFT results of the anistropic (Figure S7c and S7d) and isotropic materials (Figure S7d and S7h) from FDTD simulations for comparison. For the isotropic materials, two regular circles can be seen in the image of the FFT results, which is different from that of the anisotropic materials. There are some differences between the simulated and actual results, mainly in the amplitude, which is caused by the accuracy of the simulation.

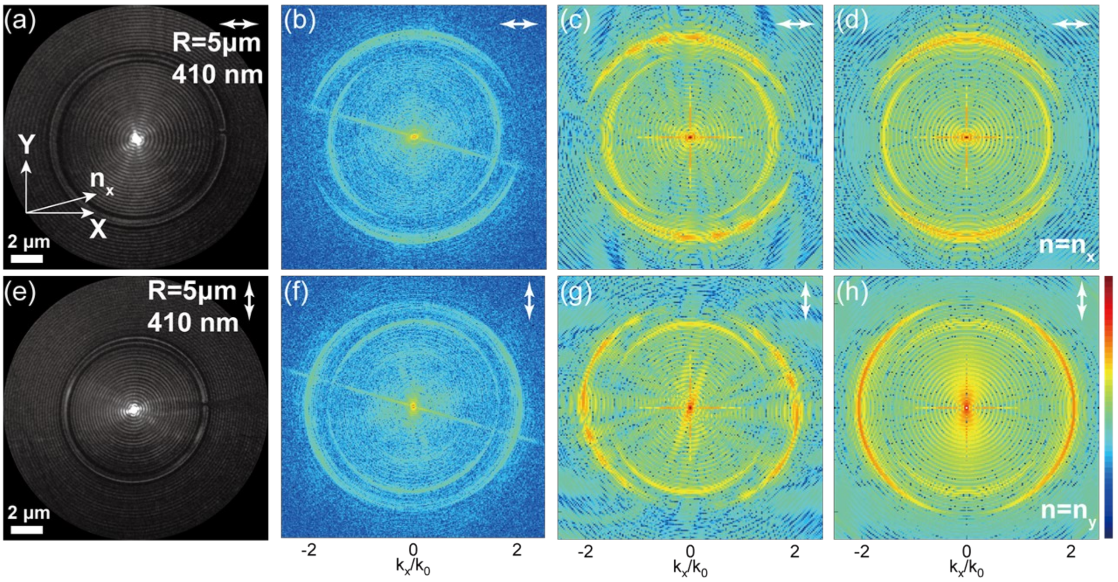

**Figure S7 FFT results of $Bi_2SeO_5$ with ring slits.** (a, e) PEEM images of $Bi_2SeO_5$ with ring slits, and the radius is 5 μm. The polarizations are shown in the insets. $\theta$ is estimated to be 15°. (b, f) FFT results of (a, b). The white dashed lines in the figure show the direction of the principal axes. (c, g) FFT results from FDTD simulations with measured refractive index. (d, h) FFT results of from FDTD results with istropic material, and the refractive index is selected to be $n_x$ and $n_y$ respectively.